Micro-mechanical analysis of composite materials using Phase-Field models of brittle fracture

Juan Macías [a,e], Albertino Arteiro [a,b], Fermín Otero [c,d], Pedro P. Camanho [a,b,*], José Reinoso [e]

[a] DEMec, Faculdade de Engenharia, Universidade do Porto, Rua Dr. Roberto Frias, s/n, Porto 4200-465, Portugal
[b] INEGI, Universidade do Porto, Rua Dr. Roberto Frias, 400, Porto 4200-465, Portugal
[c] CIMNE, Universitat Politècnica de Catalunya, Barcelona 08034, Spain
[d] Department of Nautical Science and Engineering, Universitat Politècnica de Catalunya, Pla de Palau 18, Barcelona 08003, Spain
[e] Departamento de Mecánica de Medios Continuos y Teoría de Estructuras, Escuela Técnica Superior de Ingeniería, Universidad de Sevilla, Camino de los Descubrimienos s/n, Sevilla 41092, Spain

ARTICLE INFO

ABSTRACT

Failure in fiber-reinforced composites is a complex phenomenon where different damage mechanisms interact and evolve through various scales. Micro-mechanical analysis using the finite element method has become an important alternative to study such failure phenomena and their interactions, by modeling explicitly the fiber, matrix, and fiber–matrix interface. In this work, the predictive capabilities of the finite element method together with the Phase-Field (PF) method for fracture has been assessed. The study compares different PF formulations, energy splits and numerical parameters, using Representative Volume Elements (RVEs) of different sizes, fiber distributions and with different Boundary Conditions (BCs). It is found that even though good approximations can be obtained and meso-scale failure envelopes for transverse loading generated, these are highly dependent on the modeling assumptions and PF parameters. The AT2 formulation combined with Amor's energy split provides the best predictions when compared with an analytical failure surface. The best fit is found for transverse shear-dominated loading, while larger differences are found for compressive loading, whose strength predictions are strongly affected by the PF formulations and energy splits. It is demonstrated that meso-scale strength is conditioned by interface properties as interface damage is the dominant failure initiation mechanism under tensile-dominated loading. On the other hand, PF parameters have a stronger influence on compressive-dominated loading. Finally, it is shown that assuming a perfect fiber–matrix interface has a strong effect on the expected meso-scale strength, as failure is markedly delayed. Accordingly, based on the present results, especial care should be taken in properly assessing all the variables involved in the modeling methodology to draw conclusions from computational micro-mechanical analyses based on the PF approach.

1. Introduction

The Phase-Field (PF) method for fracture results from the seminal work of Francfort and Marigo (1998) as the redefinition of Griffith's differential energy balance into an energy balance expressed in a variational integral form. Such balance defines the total potential energy as the sum of the external work, the strain energy due to elastic deformation and the crack surface integral that represents the work required to generate a crack surface. Bourdin et al. (Bourdin et al., 2000; Francfort et al., 2008) used the variational formulation and, through a damage-like variable, defined a regularized crack representation where the surface integral on the unknown crack path can be replaced by a volume integral within a diffuse damaged zone whose size is given according to a length scale parameter. The PF method has

gained increased popularity in the field of computational fracture mechanics because of the several advantages when compared with other methodologies, namely, (i) it offers the possibility of capturing fracture initiation which is not possible for methods such as the Virtual Crack-Closure Technique (VCCT); (ii) PF allows to model crack propagation without the need to use predefined crack paths or re-meshing, which are typical limitations of cohesive zone models and VCCT respectively; (iii) PF can capture crack branching and merging in 3D as well as 2D models without the need of ad hoc propagation criteria which are commonly used in XFEM and VCCT; in addition, (iv) PF can reduce the strong mesh dependency of traditional Continuum Damage Models (CDM) (Bourdin et al., 2000; Francfort et al., 2008). Thanks to these capabilities, the PF method is currently used in an extensive range

---

* Corresponding author at: DEMec, Faculdade de Engenharia, Universidade do Porto, Rua Dr. Roberto Frias, s/n, Porto 4200-465, Portugal.
E-mail addresses: macias@fe.up.pt (J. Macías), pcamanho@fe.up.pt (P.P. Camanho).

of applications, from fracture in ceramic, geological materials, metals and polymers to functionally graded material and anisotropic materials such as composite laminates (Wu et al., 2019). The introduction of PF to model fracture in composite materials was initially performed at the meso-scale (Quintanas-Corominas et al., 2019), namely at the lamina level. The PF approach to fracture was later introduced within the context of micro-mechanical analysis, from the work on a single fiber embedded in a large square matrix (Guillén-Hernández et al., 2019), to the analysis of the transverse failure of Representative Volume Elements (RVEs) (Espadas-Escalante et al., 2019) and embedded cell models (Tan and Martínez-Pañeda, 2022).

The use of PF on a single fiber embedded in a large square matrix (Guillén-Hernández et al., 2019; Zhang et al., 2019, 2020; Song et al., 2020) is limited to linear-elastic material formulations, infinitesimal deformations and neglects residual stresses. Crack kinking is always studied under the plane-strain assumption, and 3D effects such as crack tunneling have only been addressed in the 3D model of Song et al. (2020). Only the work of Guillén-Hernández et al. (2019) and Song et al. (2020) consider realistic micro-scale dimensions. The work of Zhang et al. (2019, 2020) is limited to fiber diameters of 0.5 mm, which are not representative of the micro-scale of technical composite materials. Experimental validation was done only in the study of Song et al. (2020). Song et al. (2020) and Zhang et al. (2019, 2020) use a geometric and a damage PF variable to define the interface and fracture within both the bulk matrix and the diffuse interface, while Guillén-Hernández et al. (2019) use PF damage only in the matrix, while cohesive damage is considered at the interface. The fiber is always considered linear elastic. Although the work of Song et al. (2020) and Guillén-Hernández et al. (2019) use the formulation without damage threshold called AT2, which implies a non-linear behavior from the beginning of the straining of the material, other authors such as Espadas- Espadas-Escalante et al. (2019) resort to formulations where the elastic threshold is defined according to the length scale parameter; this formulation is called AT1. There are also formulations such as that proposed by Zhang et al. (2019, 2020) where a modification of the Phase-Field cohesive zone model (PF-CZM) developed by Wu and Nguyen (2018) is used to reduce the length scale to micro-scale dimensions while defining an elastic threshold based on energy criteria instead of the length scale parameter.[1]

The work on RVE analysis using PF fracture is very limited if compared to the studies using continuum damage models. The first author that performed micro-mechanical analyses of fracture in composite materials using PF was Espadas-Escalante et al. (2019) in 2019. They used a 2D plane-strain model with an AT1 formulation and compared the performance of Amor's and Miehe's energy splits[2] in the predictive capabilities of fracture under pure tension and pure compression. Fiber-matrix interaction was assumed as perfectly bonded, and validation was performed by comparing tensile transversal strength, obtained from previously calibrated models, with the value obtained from the experimental results in Hinton et al. (2004) and the transverse compressive stress–strain curve also in Hinton et al. (2004). This model was followed by the work of Yin and Zhang (2019), where a 3D model using an AT2 formulation was used to evaluate the influence of fiber orientation on the transverse strength of a composite material. Also in this case, fiber–matrix interface damage was not considered. The results were not validated because the specimen and fiber dimensions were not representative of micro-scale dimensions. The most recent work is that of Li et al. (2020) and Zhang et al. (2020), which consider a diffuse fiber–matrix interface using a geometric PF variable. Li et al. (2020) use a 2D Von Mises plasticity model coupled with an AT2 formulation, but neither the material properties nor the fiber dimensions are representative of the micro-scale in a polymer-based composite. On the

other hand, the analysis of Zhang et al. (2020) uses a 3D model with different volume fractions and fiber distributions to study fracture in transverse tension. The formulation in this work is a modification of the PF cohesive zone model developed by Wu and Nguyen (2018), again driven by the need to reduce the length scale to fractions of the fiber diameter. So far, there have not been studies of the capabilities of PF for the prediction of failure envelopes, nor the influence of the Boundary Conditions (BCs) and RVE size on the accuracy of PF-based formulations. Also, up to this moment, PF with elastic and Von Mises plasticity formulations have been always used to account for fracture in the matrix or within the diffuse interface, because in transverse loading the fiber is not expected to damage. However, there are no micro-mechanical analyses using pressure-dependent plasticity models, which are considered of primal importance in the study of polymer matrices (Melro et al., 2013).

The in-situ effect was analyzed using PF by Guillén-Hernández et al. (2020), and the R-curve of pre-notched specimens was studied with a different PF formulation by Tan and Martínez-Pañeda (2022, 2021). The study of the in-situ effect of Guillén-Hernández et al. (2020) uses a standard AT2 linear-elastic formulation for damage in the matrix and cohesive elements in the fiber–matrix interface. This work was based on and compared with the experimental results of Saito et al. (2012). Tan and Martínez-Pañeda (2022, 2021) studied the R-curve in pre-notched specimens under three-point bending using the AT1 linear-elastic formulation to capture matrix fracture and cohesive surface interactions to model fiber–matrix decohesion. The studies are validated by comparison with the experimental results of Canal et al. (2012). In addition, the only study that considers 3D effects and fiber fracture in micro-mechanical studies of composite materials is the work of Tan and Martínez-Pañeda (2022), one of the first steps in modeling more realistic composite geometries, which can potentially be extended to the study of crack tunneling and other more complex loading scenarios.

According to the literature, for the micro-mechanical analysis of composite materials using PF fracture, there is no general trend on the methodologies and assumptions that should be considered. These tend to deviate from each other, but there is no qualitative comparison of the accuracy of each methodology. Thus, there is still the need to better understand the capabilities and limitations of the different PF methodologies for the analysis of the micro-mechanical behavior of composite materials with a more rigorous approach. For this reason, this work starts with an introduction to PF fracture. Then, the analysis of the accuracy of the different PF formulations and energy splits under different micro-structures and loading conditions is presented. This is done first with a study of the influence of the RVE size and fiber distribution on the predicted strength and strain at maximum stress. Later, using different fiber distributions, a quantitative analysis compares the PF predictions with the failure envelopes generated with the failure criteria proposed by Camanho et al. (2015). After that, the influence of the formulation and length scale parameter is also analyzed by comparing the evolution of fracture patterns and failure envelopes as the length scale parameter increases in both AT1 and AT2 formulations. Finally, the influence of considering interface damage has been discussed by comparing the increased meso-scale strength when interface damage is suppressed. The document ends with the conclusions and suggestions for future work.

2. Phase-Field method for fracture

In this section, the derivation of the PF constitutive equations is presented in a general way and then the particularities of the most common PF formulations (i.e. AT1, AT2, and PF-CZM) are detailed.

---

[1] A detailed explanation of the different formulations is given in Section 2.7.
[2] A detailed explanation of the different energy splits is given in Section 2.8.
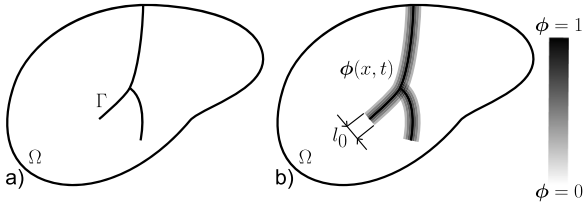
Fig. 1. Schematic representation of a solid body with (a) an internal discrete discontinuity, and (b) a Phase-Field approximation of the same discontinuity.

2.1. Griffith thermodynamic balance

The PF method for fracture is based on the thermodynamical analysis made by Griffith in Griffith (1921), where, according to the first law of thermodynamics, crack growth can only occur if such a process implies that the total energy of the system either decreases or remains constant with an increase in the crack area. In this context, a critical condition for crack propagation is defined (under equilibrium conditions) as the scenario where there is no change in total energy (Navidtehrani et al., 2021a). Thus, the Griffith principle is a local (differential) minimum for the total energy Π, based on the variation of Π with respect to the increment of the crack area dA as expressed in Eq. (1):

$$\frac{d\Pi}{dA} = \frac{d\Psi_0}{dA} + \frac{dW_c}{dA} - \frac{dW_{ext}}{dA} \tag{1}$$

where Ψ_0 is the internal strain energy, W_{ext} is the work done by the external forces, and W_c is the energy required to create new surfaces, whose variation with respect to the incremental crack area is known as the critical energy release rate $G_c = dW_c/dA$.

2.2. Variational form of the Griffith thermodynamic balance

The differential expression in Eq. (1) can be expressed in a variational form as explained by Bourdin et al. (2000) and Francfort et al. (2008), according to Eq. (2):

$$\Pi(\mathbf{u}) = \int_\Omega \Psi_0(\mathbf{u})d\Omega + \int_\Gamma G_c dS - W_{ext}(\mathbf{u}) \tag{2}$$

This equation is given within the domain defined by the pre-cracked body $\Omega \subset \mathbb{R}^n$, $n \in [1, 2, 3]$, where the internal discontinuity contour is defined by Γ and the displacement field is defined by the vector $\mathbf{u}$, see Fig. 1(a).

Within the framework of the calculus of variations, the displacement field should be found by minimizing the total energy described in Eq. (2), but as the crack path is also an unknown, the solution to the variational problem posed by Eq. (2) can become extremely complex (Wu et al., 2019). To reduce the difficulty of tracking the actual crack path, Bourdin et al. (2000) and Francfort et al. (2008) proposed a regularized version of the crack surface using an auxiliary damage-like variable ϕ. Thus, the sharp crack topology is replaced by a diffuse damaged zone of finite dimensions, controlled by a length scale parameter l_0. Then, according to Bourdin et al. (2000) and Francfort et al. (2008), the total energy $\Pi(\mathbf{u})$ in Eq. (2) can be approximated by $\Pi(\mathbf{u}, \phi)$ defined in Eq. (3):

$$\Pi(\mathbf{u}) \approx \Pi(\mathbf{u}, \phi) = \int_\Omega \Psi(\mathbf{u}, \phi)d\Omega + \int_\Omega G_c \gamma(\phi; \nabla\phi)d\Omega - W_{ext}(\mathbf{u}) \tag{3}$$

where $\Psi(\mathbf{u}, \phi)$ is the degraded internal energy and $G_c \gamma(\phi; \nabla\phi)$ is the regularized fracture energy; these are explained in detail in the following subsections.

2.3. Crack surface density function

The surface energy in Eq. (2), initially computed in the specific crack path is now approximated in a damaged zone of finite width (see Fig. 1(b)) according to Eq. (4):

$$\int_\Gamma G_c dS \approx \int_\Omega G_c \gamma(\phi; \nabla\phi)d\Omega$$

$$\gamma(\phi; \nabla\phi) = \left(\frac{\alpha(\phi)}{l_0} + l_0 |\nabla\phi|^2 \right) \tag{4}$$

where $\gamma(\phi; \nabla\phi)$ is known as the crack surface density functional given in terms of the PF variable ϕ, its gradient $\nabla\phi$ and the length scale parameter l_0. The integral term is also called the dissipated energy, because in the balance Eq. (2), the external work $W_{ext}(\mathbf{u})$ exerted on the body can either be stored as accumulated strain energy $\int_\Omega \Psi_0(\mathbf{u})d\Omega$ or dissipated in the form of surface energy due to fracture $\int_\Gamma G_c dS$.

2.4. Geometric crack function

The total dissipated (or fracture) energy described in Eq. (4) can also be given in terms of regularized damage models as explained in Marigo et al. (2016). Hence, the regularized term $\int_\Omega G_c \gamma(\phi; \nabla\phi)d\Omega$ is divided into local (depending on ϕ) and non-local (depending on $\nabla\phi$) contributions as shown in Eq. (5):

$$\int_\Omega G_c \gamma(\phi; \nabla\phi)d\Omega = \frac{G_c}{4C_w} \int_\Omega \left(\frac{\alpha(\phi)}{l_0} + l_0 |\nabla\phi|^2 \right) d\Omega \tag{5}$$

where $\alpha(\phi)$ is known as the geometric crack function, which defines the spatial distribution of the damage variable $\phi = \phi(\mathbf{x})$ in the domain Ω, and C_w is a normalization parameter that guaranties the same energy dissipation regardless of the PF formulation (see Eq. (6)).

$$C_w = \int_0^1 \sqrt{\alpha(\xi)}d\xi \tag{6}$$

If the material has not been damaged $\phi = 0$, there is no dissipated energy $\alpha(0) = 0$, and when damage reaches its maximum value $\phi = 1$, the local dissipation also reaches its maximum $\alpha(1) = 1$. Additionally, it is required that $\frac{\partial \alpha(\phi)}{\partial \phi}$ must be non-negative in order to ensure an always increasing fracture energy dissipation; $\frac{\partial \alpha(\phi)}{\partial \phi} < 0$ would imply healing of the crack, which is thermodynamically inconsistent.

2.5. Energy degradation function

According to the formulation of Continuum Damage models, the strain energy should be degraded with the evolution of the damage variable. Hence, the strain energy term $\int_\Omega \Psi(\mathbf{u})d\Omega$ must be modified accordingly to yield Eq. (7):

$$\int_\Omega \Psi_0(\mathbf{u})d\Omega \approx \int_\Omega \Psi(\mathbf{u}, \phi)d\Omega$$

$$\int_\Omega \Psi(\mathbf{u}, \phi)d\Omega = \int_\Omega [g(\phi)\Psi^+(\mathbf{u}) + \Psi^-(\mathbf{u})]d\Omega \tag{7}$$

where $g(\phi)$ is called the energetic degradation function, and $\Psi^+(\mathbf{u})$ and $\Psi^-(\mathbf{u})$ are the positive and negative contributions to the strain energy. The energy split is performed in order to avoid fracture under dominant compressive stresses.

For an undamaged material ($\phi = 0$) all the external work is stored as strain energy; thus, $g(0) = 1$. On the other hand, when the material is completely damaged ($\phi = 1$) it loses all its load-carrying capacity $g(1) = 0$; besides, this function should be a decreasing function, $\frac{\partial g(\phi)}{\partial \phi} \leq 0$, such that the evolution of damage can only decrease the internal energy.

2.6. Euler equations (strong form)

Considering that the work of external forces can be expressed as the sum of surface tractions $\mathbf{t}^*$ on the part of the boundary $\partial\Omega_t$, and body forces $\mathbf{b}^*$ over the volume of the body Ω, the external work can be rewritten as:

$$W_{ext}(\mathbf{u}) = \int_{\partial\Omega_t} (\mathbf{t}^* \cdot \mathbf{u}) \mathrm{d}\partial\Omega + \int_\Omega (\mathbf{b}^* \cdot \mathbf{u}) \mathrm{d}\Omega \tag{8}$$

Therefore, by using Eqs. (4), (5), (7), and (8), the total energy functional in Eq. (2) can be rewritten as:

$$\Pi(\mathbf{u}, \boldsymbol{\phi}) = \int_\Omega \Psi(\mathbf{u}, \boldsymbol{\phi}) \mathrm{d}\Omega$$
$$+ \frac{G_c}{4C_w} \int_\Omega \left(\frac{\alpha(\boldsymbol{\phi})}{l_0} + l_0 |\nabla\boldsymbol{\phi}|^2 \right) \mathrm{d}\Omega \tag{9}$$
$$- \int_{\partial\Omega_t} (\mathbf{t}^* \cdot \mathbf{u}) \mathrm{d}\partial\Omega - \int_\Omega (\mathbf{b}^* \cdot \mathbf{u}) \mathrm{d}\Omega$$

According to the calculus of variations, the actual displacement $\mathbf{u} = \mathbf{u}(\mathbf{x})$ and PF variable $\boldsymbol{\phi} = \boldsymbol{\phi}(\mathbf{x})$ fields are the stationary functions of the total energy functional in Eq. (9), which can be found by setting the variation of $\Pi(\mathbf{u}, \boldsymbol{\phi})$ with respect to $\mathbf{u}$ and $\boldsymbol{\phi}$ equal to zero and then applying the divergence theorem to obtain Eq. (10):

$$\delta\Pi(\mathbf{u}, \boldsymbol{\phi}) = -\int_\Omega \left[\nabla \cdot \left(\frac{\partial\Psi(\mathbf{u}, \boldsymbol{\phi})}{\partial\boldsymbol{\epsilon}(\mathbf{u})} \right) + \mathbf{b}^* \right] \cdot \delta\mathbf{u} \mathrm{d}\Omega$$
$$+ \int_{\partial\Omega_t} (\boldsymbol{\sigma} \cdot \mathbf{n} - \mathbf{t}^*) \cdot \delta\mathbf{u} \mathrm{d}\partial\Omega$$
$$+ \int_\Omega \left[\frac{\partial\Psi(\mathbf{u}, \boldsymbol{\phi})}{\partial\boldsymbol{\phi}} + G_c \left(\frac{\partial\gamma}{\partial\boldsymbol{\phi}} - \nabla \cdot \left(\frac{\partial\gamma}{\partial\nabla\boldsymbol{\phi}} \right) \right) \right] \cdot \delta\boldsymbol{\phi} \mathrm{d}\Omega \tag{10}$$
$$+ \int_{\partial\Omega} Gc \left(\frac{\partial\gamma}{\partial\nabla\boldsymbol{\phi}} \cdot \mathbf{n} \right) \delta\boldsymbol{\phi} \mathrm{d}\partial\Omega$$

where $\mathbf{n}$ is the outward normal vector.

From Eq. (10), the Euler equations or strong form can be extracted as a coupled system of differential equations:

$$\nabla \cdot \left(\frac{\partial\Psi(\mathbf{u}, \boldsymbol{\phi})}{\partial\boldsymbol{\epsilon}(\mathbf{u})} \right) + \mathbf{b}^* = \mathbf{0} \quad \text{in} \quad \Omega$$
$$\frac{\partial\Psi(\mathbf{u}, \boldsymbol{\phi})}{\partial\boldsymbol{\phi}} + G_c \left(\frac{\partial\gamma}{\partial\boldsymbol{\phi}} - \nabla \cdot \left(\frac{\partial\gamma}{\partial\nabla\boldsymbol{\phi}} \right) \right) = 0 \quad \text{in} \quad \Omega \tag{11}$$

with the boundary conditions:

$$\boldsymbol{\sigma} \cdot \mathbf{n} = \mathbf{t}^* \quad \text{on} \quad \partial\Omega_t$$
$$\nabla\boldsymbol{\phi} \cdot \mathbf{n} = \mathbf{0} \quad \text{on} \quad \partial\Omega \tag{12}$$

The term $\frac{\partial\Psi(\mathbf{u}, \boldsymbol{\phi})}{\partial\boldsymbol{\phi}}$ is called the energetic crack driving force, and it can be expressed as:

$$\frac{\partial\Psi(\mathbf{u}, \boldsymbol{\phi})}{\partial\boldsymbol{\phi}} = \frac{\partial\Psi(\mathbf{u}, \boldsymbol{\phi})}{\partial g(\boldsymbol{\phi})} \frac{\partial g(\boldsymbol{\phi})}{\partial\boldsymbol{\phi}} = \Psi^+(\mathbf{u}) \frac{\partial g(\boldsymbol{\phi})}{\partial\boldsymbol{\phi}} \tag{13}$$

Also, the terms $\frac{\partial\gamma}{\partial\nabla\boldsymbol{\phi}}$ and $\frac{\partial\gamma}{\partial\boldsymbol{\phi}}$ can be simplified as shown in Eq. (14):

$$\frac{\partial\gamma}{\partial\nabla\boldsymbol{\phi}} = \frac{l_0}{2C_w} |\nabla\boldsymbol{\phi}|$$
$$\frac{\partial\gamma}{\partial\boldsymbol{\phi}} = \frac{1}{4C_w l_0} \frac{\partial\alpha(\boldsymbol{\phi})}{\partial\boldsymbol{\phi}} \tag{14}$$

2.7. Phase-Field formulations

The particular forms of the normalization parameter C_w, degradation function $g(\boldsymbol{\phi})$ and geometric functions $\alpha(\boldsymbol{\phi})$ define the specific PF formulations. The most popular are: (i) the AT1 model which uses a quadratic degradation function and a linear geometric function, (ii) the AT2 model which uses quadratic functions for both geometric and degradation functions (the main difference between these two models resides in the geometric crack function) and (iii) the Phase-Field Cohesive zone model (PF-CZM) which uses a quadratic geometric

Table 1
Geometric and degradation functions for AT1, AT2 and PF-CZM models (Wu et al., 2019).

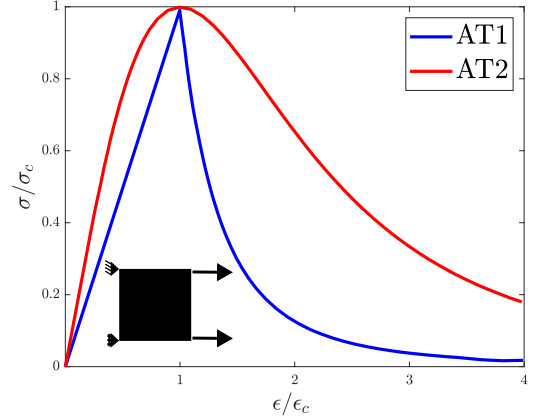| Model	$\alpha(\boldsymbol{\phi})$	$g(\boldsymbol{\phi})$	C_w	l_0
AT1	$\boldsymbol{\phi}$	$(1-\boldsymbol{\phi})^2$	2/3	$\frac{8G_c E}{3\sigma_c^2}$
AT2	$\boldsymbol{\phi}^2$	$(1-\boldsymbol{\phi})^2$	1/2	$\frac{27G_c E}{256\sigma_c^2}$
PF-CZM	$2\boldsymbol{\phi} - \boldsymbol{\phi}^2$	$\frac{(1-\boldsymbol{\phi})^p}{(1-\boldsymbol{\phi})^p + Q(\boldsymbol{\phi}.)}$	$\pi/4$	[−]

Fig. 2. Stress–strain behavior for AT1 and AT2 models in a single finite element under tension (Kristensen et al., 2021), where σ_c is the strength and ϵ_c is the strain when the stress reaches σ_c.

function and a rational degradation function (Wu et al., 2019, chap. 3), see Table 1. AT1 and PF-CZM present linear-elastic behavior up to the maximum stress while AT2 has the particularity $\frac{\partial\alpha}{\partial\boldsymbol{\phi}}(\boldsymbol{\phi} = 0) = 0$ which enforces non-linear behavior prior to the predefined strength is reached, see Fig. 2. In the AT1 and AT2 models, the PF length scale parameter is used to control the material strength (σ_c) and can be related to the material properties according to the 1D analytical solution of the PF differential equations (weak form) described in Eqs. (11). Conversely, in the PF-CZM model the strength is explicitly defined and it does not depend on the length scale parameter.

Throughout the progressive loading, the PF variable approaches one, and the degradation function tends to zero. This imposes a zero stiffness in the material that can create numerical instabilities and an ill-posed tangent matrix. This is why some authors (Navidtehrani et al., 2021a; Martínez-Pañeda et al., 2018; Navidtehrani et al., 2021b) recommend using a modified version of the degradation function for AT1 and AT2 models, see Eq. (15), where κ is a very small positive number.

$$g(\boldsymbol{\phi}) = (1-\boldsymbol{\phi})^2 + \kappa \tag{15}$$

2.8. Strain energy split

As mentioned before, fracture under dominated compressive stresses is precluded by means of a decomposition of the strain energy into active $\Psi^+(\mathbf{u})$ and inactive $\Psi^-(\mathbf{u})$ contributions (see Eq. (7)). The most common decomposition methods for infinitesimal elasticity formulations are: the volumetric-deviatoric split of Amor et al. (2009) (see Eq. (16)) and the spectral decomposition of Miehe et al. (2010) (see Eq. (17)). These decompositions apply only to the AT1 and AT2 formulations. The default decomposition used in PF-CZM is the one shown in Eq. (18).

$$\Psi^-(\boldsymbol{\epsilon}(\mathbf{u})) = \frac{K}{2} \mathrm{tr}^-(\boldsymbol{\epsilon}(\mathbf{u}))$$
$$\Psi^+(\boldsymbol{\epsilon}(\mathbf{u})) = \frac{K}{2} \mathrm{tr}^+(\boldsymbol{\epsilon}(\mathbf{u})) + \mu\boldsymbol{\epsilon}_D(\mathbf{u}) : \boldsymbol{\epsilon}_D(\mathbf{u}) \tag{16}$$

$$\Psi^{\pm}(\epsilon(\mathbf{u})) = \frac{K}{2}\langle\epsilon_1(\mathbf{u}) + \epsilon_2(\mathbf{u}) + \epsilon_3(\mathbf{u})\rangle_{\pm}^2 +$$
$$\mu(\langle\epsilon_1(\mathbf{u})\rangle_{\pm}^2 + \langle\epsilon_2(\mathbf{u})\rangle_{\pm}^2 + \langle\epsilon_3(\mathbf{u})\rangle_{\pm}^2) \tag{17}$$

$$\Psi^+(\sigma(\mathbf{u})) = \frac{\langle\sigma_1(\mathbf{u})\rangle_+^2}{2E}$$

$$\Psi^-(\sigma(\mathbf{u})) = \frac{1}{2E}\left[\sigma_1(\mathbf{u})\langle\sigma_1(\mathbf{u})\rangle_- + \right.$$
$$\sigma_2(\mathbf{u})^2 + \sigma_3(\mathbf{u})^2 - \tag{18}$$
$$\left. 2\nu\left(\sigma_2(\mathbf{u})\sigma_3(\mathbf{u}) + \sigma_1(\mathbf{u})\sigma_3(\mathbf{u}) + \sigma_1(\mathbf{u})\sigma_2(\mathbf{u})\right)\right]$$

Here, K and μ are the elastic Lamé parameters, E is the Young's modulus, ν is the Poisson's ratio, $\epsilon(\mathbf{u})$ is the infinitesimal strain tensor, ϵ_D is the deviatoric part of the infinitesimal strain tensor, $\sigma(\mathbf{u})$ is the Cauchy stress, $\sigma_i(\mathbf{u})$ are the principal stresses and $\langle\rangle$ is the Macaulay operator.

Any particular form of the energy split applied in the balance of linear momentum as well as the PF balance (Eqs. (11)) leads to the so-called "anisotropic" PF formulation, because when damage progresses, the material response under compression and tension is different, and the material is no longer isotropic. The use of the energy split in the PF balance only renders the so-called "hybrid" formulation.

2.9. Damage irreversibility

The damage irreversibility condition ($\dot{\phi} \geq 0$) is ensured by using a local history variable H that satisfies the fracture Karush–Kuhn–Tucker conditions in Eq. (19). H is defined in Eq. (20).

$$\Psi^+ - H \leq 0, \dot{H} \geq 0, \dot{H}(\Psi^+ - H) = 0 \tag{19}$$

$$H = \mathbf{max}_{\tau\in[0,t]}\Psi^+(\tau) \tag{20}$$

2.10. Phase-Field balance equations

The strong form in Eq. (11) is rewritten using the definition of the energetic crack driving force in Eq. (13) and the history variable defined in Eq. (20), to define the balance equations of the PF method in Eq. (21), under the same boundary conditions defined in Eq. (12).

$$\nabla\cdot\left(\frac{\partial\Psi(\mathbf{u},\phi)}{\partial\epsilon(\mathbf{u})}\right) + \mathbf{b}^* = \mathbf{0} \quad \text{in} \quad \Omega$$
$$H\frac{\partial g(\phi)}{\partial\phi} + \frac{G_c}{2c_w}\left(\frac{1}{2l_0}\frac{\partial\alpha(\phi)}{\partial\phi} - l_0\nabla\cdot|\nabla\phi|\right) = 0 \quad \text{in} \quad \Omega \tag{21}$$

2.11. Solution scheme

In the coupled system of Eqs. (21) the displacements and PF variable are both unknown. When this system is discretized and linearized using the Newton–Raphson method, it can be solved using two different approaches. If the displacements and PF variable are solved simultaneously, the solution method is called *"monolithic"*, a method that does not depend on the size of the time step increment, but the solution is non-convex, which may lead to convergence issues (Wu and Huang, 2020). In the *"monolithic"* scheme, convergence can be improved by using quasi-Newton methods, as was shown by Wu and Huang (2020) using the PF-CZM formulation and by Kristensen and Martínez-Pañeda (2020) using AT1 and AT2 formulations. On the other hand, the system of Eqs. (21) can be solved by iteratively freezing displacements and solving for the PF variable, then freezing the PF variable and solving for displacements, this solution method is called *staggered*, in this case, the solution depends on the size of the time increment, therefore it requires convergence studies on the time step. When the system of Eqs. (21) is decoupled, both PF and displacement problems become convex with respect to each variable; this is why convergence in the *staggered* scheme is often ensured (Wu and Huang, 2020).

Table 2
Material properties of the fibers, matrix and fiber–matrix interface used in linear-elastic AT1 and AT2 formulations for micro-mechanical numerical analysis. Fiber and matrix properties are obtained from Camanho et al. (2015), interface properties are taken from Arteiro et al. (2014) and the value of G_c for the epoxy matrix is obtained from Guillén-Hernández et al. (2020).

Matrix			
E [MPa]	ν [–]	l_0 [mm]	G_c [N/mm]
3760	0.39	0.001	0.02
Fibers			
E [MPa]	ν [–]		
74000	0.2		
Interface			
K_I [N/mm^3]	K_{II} [N/mm^3]	σ_{0I} [MPa]	σ_{0II} [MPa]
10^8	10^8	50.0	75.0
G_{Ic} [N/mm]	G_{IIc} [N/mm]	BK law [–]	
0.002	0.006	1.45	

3. Materials and interaction models

In this work, the models use micro-scale dimensions where the fibers are 5 μm in diameter (typical of carbon and E-Glass fibers in thin-ply composites). The fiber distributions within the RVE and embedded cell models are generated using the random sequential absorption method already included in the software Digimat (Anon, 2022). The material and interface properties in all scenarios are those shown in Table 2, extracted from the micro-mechanical simulations used to cross-validate the failure criteria by Camanho et al. (2015), and from Arteiro et al. (2014) and Guillén-Hernández et al. (2020).

This work seeks to explore the accuracy of the AT1 and AT2 formulations combined with the different energy splits in comparison with meso-scale failure criteria. Therefore, in these formulations, the material strength is controlled by the length scale parameter l_0, which is set to 0.001 mm for the linear-elastic AT1 and AT2 formulations. This yields a higher matrix strength than that given in Camanho et al. (2015). Camanho et al. (2015) used a matrix tensile strength of 93 MPa. This would imply a length scale of 0.0038 mm for AT1 and 0.00108 mm for AT2. But there is a geometrical limitation given by the fiber dimensions, related to the fact that there is a minimum length scale required to simulate crack localization, which can also be promoted, or prevented, by the boundary conditions and even the energy split. The length scale can be gradually reduced to achieve a more crack-like fracture pattern, but it would come at the cost of a potential overestimation of the material strength. This shows that for standard PF formulations there is a geometrical bias imposed by the micro-scale dimensions on the length scale parameter that can influence the material strength.

In all cases, the UEL Abaqus implementation described in Martínez-Pañeda et al. (2018) is used for 2D plane strain elements under infinitesimal deformation assumptions. To overcome convergence issues, the *staggered* solution scheme is used, following a sensitivity study of the minimum required time step to obtain time-step independent results previously to all analyses. Besides, the studies of the different energy splits were done using a "hybrid" implementation. The geometries and loading are such that the analysis is performed in the direction transverse to the fiber, so only transverse normal loading and shear are applied (22, 33 and 23 directions). Cohesive surface interaction is used to model fiber–matrix interface damage with a bilinear behavior and the Benzeggagh–Kenane (BK) fracture criteria. The surface interaction also accounts for normal contact after complete decohesion but without considering friction.

4. RVE analysis

For the RVE analysis, a study on the RVE size is initially performed to estimate the dimensions required to obtain representative strengths

and maximum strain values. The study is performed with RVEs with 60% fiber volume fraction and the properties shown in Table 2. Once the minimum size is defined, a comparative study using the results of the analytical model of Camanho et al. (2015) is used to verify the predictive capabilities of the different energy splits and PF formulations. The influence of the length scale parameter and interface cohesive interaction is also analyzed in order to verify the accuracy of all the assumptions within this methodology.

4.1. RVE size study

To estimate the minimum size that can be used and to obtain meaningful strength and maximum strain measurements, transverse tensile loads are applied on square RVEs of side length from 0.02 mm (RVE size equivalent to the one used by Espadas-Escalante et al., 2019) to 0.08 mm, or from a ratio $L/r_{fiber} = 8$ to $L/r_{fiber} = 32$, where L is the length of the sides of the RVE and r_{fiber} is the fiber radius, see Fig. 3. In this example, only the AT1 formulation with Miehe's energy split is used. For each value of L/r_{fiber}, six different random distributions are generated and simulated. From that, average, minimum and maximum values of strength and strain at peak stress are plotted in Fig. 4 and Fig. 5 respectively. The values of strength and strain at peak stress for the largest RVEs where no evident variation is obtained by increasing the size of the RVE are called "asymptotic values", which are considered to be the most accurate approximation obtained.

The strength predictions do not match the strength predicted by Camanho et al. (2015) using computational micro-mechanics. An overestimation of 8.28% is observed even for the largest RVEs. Nevertheless, it can be seen from Figs. 4 and 5 that the scatter of the strain and strength distributions narrows down as the size of the RVE increases. In addition, the average value has an asymptotic behavior with the increase of the RVE size. This behavior is expected as it follows the trend observed in the results of van der Meer (2016). The results presented in van der Meer (2016) showed that the variation of the average strain from a small RVE to the asymptotic value can reach 7% which is still lower than the variation obtained by RVEs of medium size. In the present results, this is also the case for the predicted strength, where a 3.6% variation of the average value with increasing RVE size is obtained. But the asymptotic value of strain at maximum stress has a 20% difference with respect to the smallest RVE size. Besides, the asymptotic value is outside the variability obtained in the smallest RVEs. This is expected as the stiffness of smaller RVEs after failure initiation is highly polluted by spurious gradual softening due to the periodic BC after damage onset. In general, these results agree with the conclusions of Trias et al. (2006), showing that different metrics require different ratios L/r_{fiber}; even though a square RVE of 0.02 mm side length can be enough for the prediction of maximum stress (average value is less than 5% different from the asymptotic value), the RVE size necessary to predict the strain to failure can be up to three times higher.

The representative stress–strain curves for each RVE size are shown in Fig. 6, which provides an overall representation of the difference in the post-peak behavior as the RVE size increases. In all stress–strain curves, the strength reported by Camanho et al. (2015) is also shown. As explained previously, smaller RVEs produce a more gradual failure, because the periodic BCs produce spurious interactions, especially if it is close to the edges of the RVE; it means that periodic BCs make a crack tip on one side to interact and even gets arrested by the tip of the same crack on the other side, see Fig. 7. This is why for small RVEs the last part of the curves in Fig. 6 have a tendency to flatten. This effect clearly diminishes with the increase of the RVE size, but the behavior is dominantly brittle only for the RVEs with $L = 0.08$ mm. These results clearly show the inadequacy of periodic BCs to model fracture in RVEs, supporting the claim of Coenen et al. (2012b) of the need for special kinematics that allow strain localization, especially within smaller RVEs.
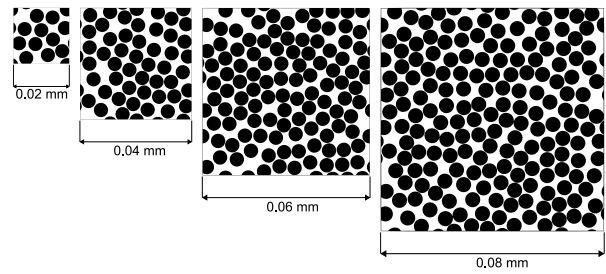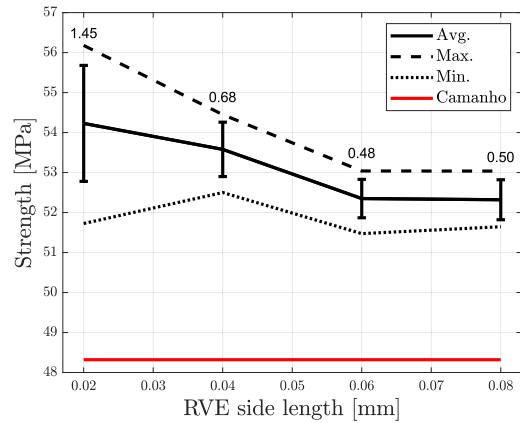

Fig. 3. RVE sizes tested in tension.

Fig. 4. Maximum, minimum, average and standard deviation (vertical bars) of the peak stress values for different RVE sizes, Phase-Field AT1 formulation and Miehe's energy split. (For interpretation of the references to color in this figure legend, the reader is referred to the web version of this article.)
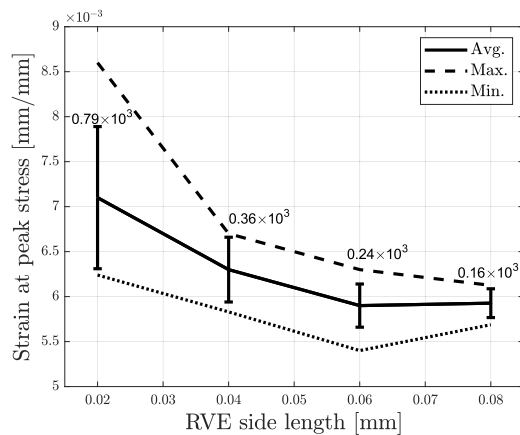

Fig. 5. Maximum, minimum, average and standard deviation (vertical bars) of the strains at peak stress for different RVE sizes, PF AT1 formulation and Miehe's energy split.

Such unrealistic post-peak behavior due to the periodic BCs renders the analysis of a single RVE of small dimensions, e.g., $L/r_{fiber} = 8$ (Espadas-Escalante et al., 2019), not necessarily representative of the meso-scale composite behavior. In fact, as is shown in the results of Fig. 6, if periodic BCs are used, the post-peak behavior is highly affected by the size of the RVE, as well as the PF formulation and energy split; see Fig. 12. In addition, if the fiber distribution is randomly generated, a large variability in post-peak behavior can be observed, especially if values of L/r_{fiber} are small, as shown in Fig. 8, where the meso-scale stress–strain curves of six RVEs with different random fiber distributions are plotted for $L/r_{fiber} = 8$ using the AT1 formulation and Miehe's split (Miehe et al., 2010). In this graph, it is shown that
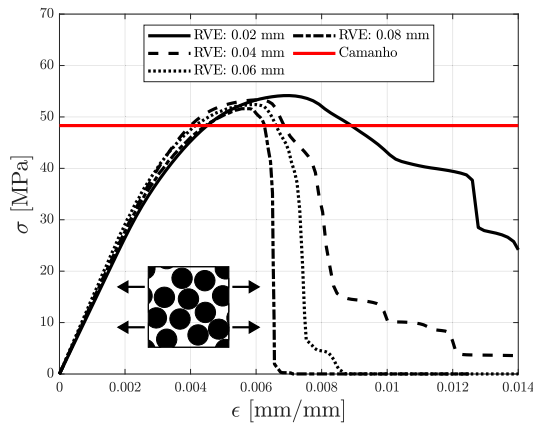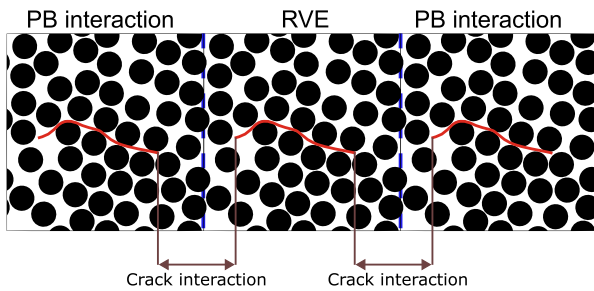
Fig. 6. Stress–strain curves for different RVE sizes, PF AT1 formulation and Miehe's energy split. (For interpretation of the references to color in this figure legend, the reader is referred to the web version of this article.)

Fig. 7. Effect of periodic boundary (PB) interaction on crack propagation.

some fiber patterns yield an "apparent" tougher material response, while others could be seen as more brittle. Another important aspect is the fact that cohesive interface damage in such small RVEs can also promote gradual failure, while assuming a perfect fiber–matrix interaction (Espadas-Escalante et al., 2019) can promote a more brittle behavior, yielding sharper stress–strain curves. Finally, it should be noted that, despite the recent efforts to define appropriate boundary conditions in the presence of localization (Coenen et al., 2012b,a; Svenning et al., 2017), the complex, interacting failure mechanisms observed in composite laminates still pose challenges to the definition of accurate boundary conditions for RVEs after localization takes place. This is a particularly relevant problem for multiscale analysis where information is transferred between different scales.

4.2. Phase-Field RVE study

According to the discussion presented in the previous section, for stress analysis, since the average strength of a square RVE of dimensions $L = 0.02$ mm is less than 5% higher than the asymptotic value, then these dimensions can be considered to give the required accuracy for the following studies. Then, the results presented Sections 4.2–4.4 correspond to the average results obtained from six different RVEs with different fiber distributions, where all RVEs have a side length of 0.02 mm. For this and the remaining analyses, the failure envelope obtained using the criteria proposed by Camanho et al. (2015) is considered the reference result, obtained solving:

$$\alpha_1 I_1 + \alpha_2 I_2 + \alpha_3 I_3 + \alpha_{32} I_3^2 - 1 = 0 \tag{22}$$

where:

$$I_1 = \frac{1}{4}\sigma_{22}^2 - \frac{1}{2}\sigma_{22}\sigma_{33} + \frac{1}{4}\sigma_{33}^2 + \sigma_{23}^2$$
$$I_2 = \sigma_{12}^2 + \sigma_{13}^2$$
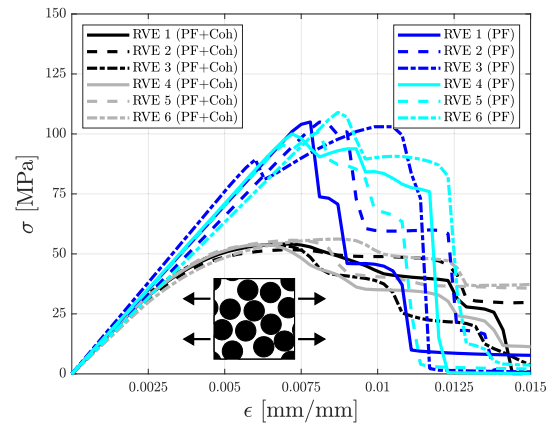$$I_3 = \sigma_{22} + \sigma_{33}$$

Fig. 8. Stress–strain curves for tension loading of RVEs of 0.02 mm size with perfect interface bonding (PF) and with cohesive interface damage (PF+Coh), AT1 formulation and Miehe's energy split. (For interpretation of the references to color in this figure legend, the reader is referred to the web version of this article.)

$$\alpha_1 = \frac{1}{S_T^2}$$
$$\alpha_2 = \frac{1}{S_L^2}$$
$$\alpha_3 = \alpha_3^t = \frac{1}{2Y_{BT}} - 2\alpha_{32}^t Y_{BT} \text{ if } I_3 > 0$$
$$\alpha_3 = \alpha_3^c = \frac{1}{2Y_{BC}} - 2\alpha_{32}^c Y_{BC} \text{ if } I_3 \leq 0$$
$$\alpha_{32} = \alpha_{32}^t = \frac{1 - \frac{Y_T}{2Y_{BT}} - \alpha_1 \frac{Y_T^2}{4}}{Y_T^2 - 2Y_{BT}Y_T} \text{ if } I_3 > 0$$
$$\alpha_{32} = \alpha_{32}^c = \frac{1 - \frac{Y_C}{2Y_{BC}} - \alpha_1 \frac{Y_C^2}{4}}{Y_C^2 - 2Y_{BC}Y_C} \text{ if } I_3 \leq 0 \text{ and } S_T \text{ and } S_L \text{ are respectively}$$

the transverse and in-plane shear strengths, Y_T and Y_C are respectively the transverse tensile and compressive strengths, and Y_{BT} and Y_{BC} are respectively the biaxial transverse tensile and compressive strengths, obtained from computational micro-mechanics (Camanho et al., 2015). This analytical model, which predicts the strength of homogenized transversely isotropic fiber-reinforced composites for multiaxial stress states, has been validated through direct comparison with experimental data from the literature for several polymer–matrix composite materials. For that reason, it is used to benchmark the predictions of the micro-mechanical simulations that employ the phase-field method to model fracture of the polymer matrix. A similar approach is proposed by Camanho et al. (2015) to perform cross-validation of the analytical model and computational micro-mechanics. Hence, in the present work, the failure criteria proposed by Camanho et al. (2015) is compared with the PF analyses using the AT1 and AT2 formulations without energy split, with Amor's split (Amor et al., 2009) and with Miehe's split (Miehe et al., 2010). In addition, a case "*Cohesive Only*" is added to delimit the area where the load drop used to estimate the composite strength is dominated by fiber–matrix decohesion. This curve is computed using RVEs where the matrix is considered linear elastic and no matrix damage is accounted for, with the load drop exclusively due to the sudden accumulation of decohesions. The purpose is to show that, if the strength of the matrix is very high due to the value of the length scale parameter, due to the formulation, or due to the energy split, the matrix behavior loses relevance because the whole phenomenon is dominated by the fiber–matrix interface strength and fracture toughness.

As explained before, a 2D plane strain model representing a transverse random fiber distribution with periodic BCs is employed, and a σ_{22}–σ_{23} loading is applied in an RVE according to Fig. 9. Similar to the previous analysis, the results presented here are the mean values from six different distributions on RVEs of the same size. The complete σ_{22}–σ_{23} failure envelopes are plotted in Fig. 10; in addition, the crack patterns and close-up observation of the intersections with the

coordinate axes are shown for pure tension in Fig. 11, pure compression in Fig. 12, and pure transverse shear in Fig. 13.

In general, the most accurate stress prediction for pure normal loading is the AT2 formulation combined with Amor's split. It gives the lower overestimation under tensile (10.1% difference) and compressive (4.4% difference) load, but the highest difference in the transverse shear strength (−4.0% difference, while all other models lead to around ±1.0% difference). All the curves are very close to each other, with differences lower than 12.0%, for tensile-dominated loading, but large deviations are observed on compressive-dominated loading, with Miehe's split always giving the highest difference; in fact, the compressive strength with Miehe's split is dominantly triggered by fiber–matrix decohesion.

If an energy split is used, the AT1 formulation overpredicts the failure envelopes of Camanho et al. (2015), especially when Miehe's split is used. On the other hand, the AT2 formulations cross the reference envelope of Camanho et al. (2015) on the shear-dominated loading, because the AT2 formulation struggles to localize fracture under shear, which generates spurious softening all over the RVE, reducing the maximum stress that can be reached; this can be observed in the crack patterns of Fig. 13. In addition, the AT2 formulation under shear loading is more prone to plastic-like fracture patterns where the crack tends to run perpendicular to the shear orientation, similar to the crack patterns in the RVE analyses of Totry et al. (2008a,b). However, if the split of Miehe et al. (2010) is used, brittle-like crack patterns can still be obtained with the AT2 formulation. On the other hand, the AT1 formulation predicts fracture along the plane of maximum principal stress, similar to what is expected from RVE analyses using pressure-dependent plasticity-damage models (Melro et al., 2013; Danzi et al., 2017; Tan et al., 2018; Sun et al., 2018) and the crack band model of Pineda et al. (2013). Under tensile-dominated loading, initial fiber–matrix decohesion promotes fracture localization; then, spurious softening is less severe and all formulations and splits give very close results in terms of stress distribution and crack patterns. They also match the fracture patterns of RVE analyses following a "*weak interfaces*" assumption (Vaughan and McCarthy, 2011), where the interface fracture toughness is significantly lower than that of the matrix (see Table 2). For tensile-dominated loading, from pure tension to pure transverse shear, failure is dominated by fiber–matrix decohesion, and all the curves are close to the "*Cohesive Only*" limit, which is dominated by the "*weak interfaces*". Due to the linear behavior of the AT1 formulation, the PF predictions match the "*Cohesive Only*", as matrix fracture is triggered after the cohesive damage instability occurred. On the other hand, due to the softening of the AT2 formulation, the stresses inside the RVE are slightly diminished before the cohesive instability is triggered.

In general, for compressive-dominated loading, the difference in the matrix strength due to the formulation and energy split plays a more important role. In this case, not accounting for an energy split implies an underestimation of the strength. If an energy split is used, the effect is the opposite, the composite strength is overpredicted, and such overestimation is increased by using Miehe's split or the AT1 formulation. The AT1 formulation combined with Amor's split, and both AT1 and AT2 formulations with no energy split yield crack patterns perpendicular to the loading direction that are considered unrealistic, in the sense that disagree with both experimental as well as previous numerical observations. Miehe's split, regardless of the formulation, and Amor's split with the AT2 formulation yield fracture angles (with respect to the normal to the load direction) clearly larger than 45°, as observed in previous numerical results (Tan et al., 2018) and in the experimental results of Puck and Schürmann (2002). If no energy split is used, the maximum compressive strength is lower than the failure envelope of Camanho et al. (2015).

From the preliminary study of fracture on the RVEs using different sizes and loading conditions, it can be concluded that the current models, alongside the assumed mechanical properties, overestimates
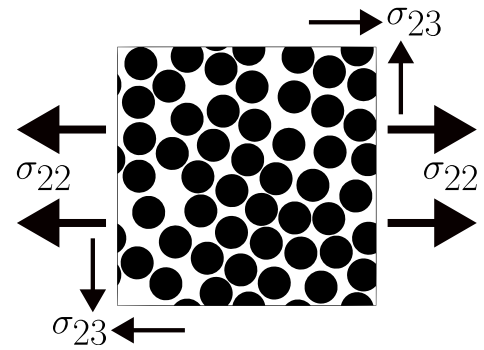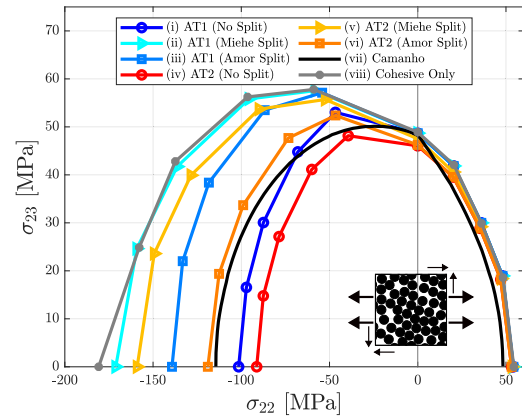
Fig. 9. RVE loading orientation.

Fig. 10. Failure envelopes of: (i) linear-elastic AT1 formulation without energy split, (ii) linear-elastic AT1 formulation with Miehe's energy split, (iii) linear-elastic AT1 formulation with Amor's energy split, (iv) linear-elastic AT2 formulation without energy split, (v) linear-elastic AT2 formulation with Miehe's energy split, (vi) linear-elastic AT2 formulation with Amor's energy split, (vii) Camanho et al. (2015) and (viii) linear-elastic matrix and cohesive interface damage (Cohesive Only). (For interpretation of the references to color in this figure legend, the reader is referred to the web version of this article.)

the meso-scale strength in tension and compression if an energy split is used, with the predictions of compressive strength yielding the highest differences. As explained in the next section, one of the most evident reasons for the overestimation is the fact that a higher strength is assumed on the resin in order to reduce the length scale parameter so that the damage pattern can actually resemble a fracture-like shape. For simulations where the length scale is further reduced, the failure surfaces are expected to enlarge proportionally up to the "*Cohesive Only*" surface limit; but, if the length scale is increased, even though a better fit could be obtained on the strength prediction, damage localization cannot be achieved, and failure could not be visualized in the form of crack formation, but rather diffuse damage. This indicates that if the length scale parameter could be interpreted as a material property associated to the material strength and fracture toughness, which is the case of the AT1 and AT2 formulations, the usability of such parameter for the specific geometric arrangement and dimensions that need to be studied in the context of computational micro-mechanics can become an important limitation on both the spatial scales that can be modeled as well as the accuracy of the results that can be obtained.

4.3. Influence of the length scale on the failure envelope

To study the effect of the length scale parameter on the transverse failure predictions, new envelopes are calculated using values of length scale equal to 1 µm, 2 µm and 3 µm; see Fig. 14. Again, the results are compared with the case "*Cohesive Only*" to assess if failure is triggered
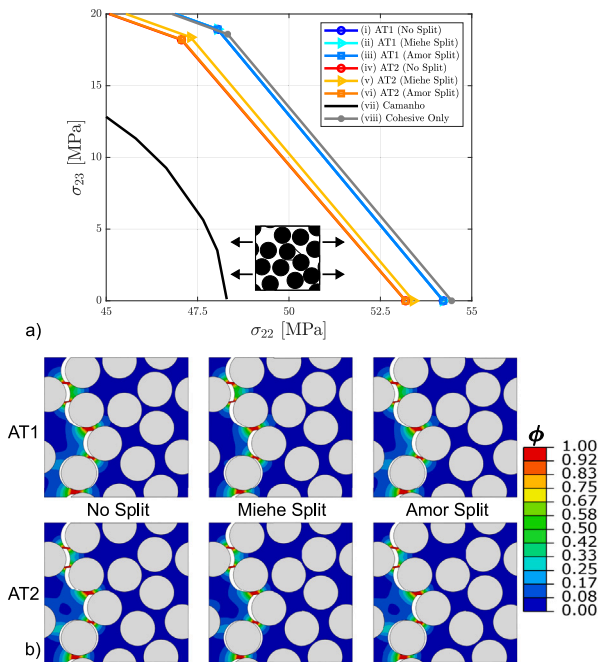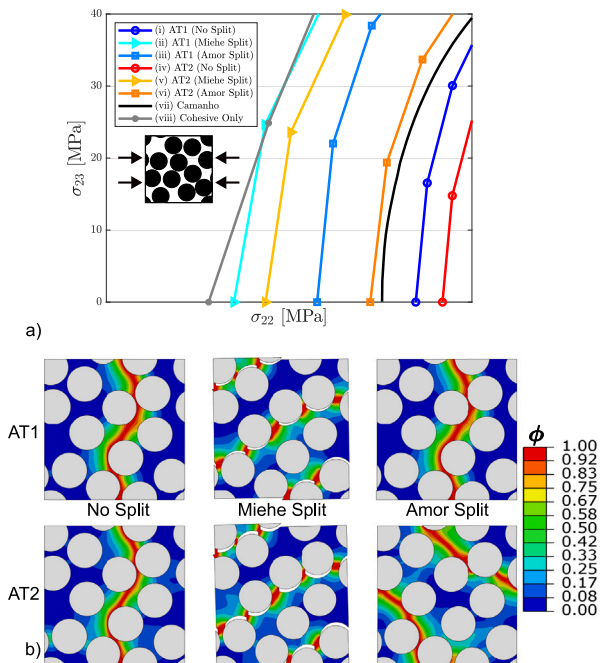
Fig. 11. (a) Failure envelopes and (b) crack patterns for pure tensile load of: (i) linear-elastic AT1 formulation without energy split, (ii) linear-elastic AT1 formulation with Miehe's energy split, (iii) linear-elastic AT1 formulation with Amor's energy split, (iv) linear-elastic AT2 formulation without energy split, (v) linear-elastic AT2 formulation with Miehe's energy split, (vi) linear-elastic AT2 formulation with Amor's energy split, (vii) Camanho et al. (2015) and (viii) linear-elastic matrix and cohesive interface damage (Cohesive Only). (For interpretation of the references to color in this figure legend, the reader is referred to the web version of this article.)
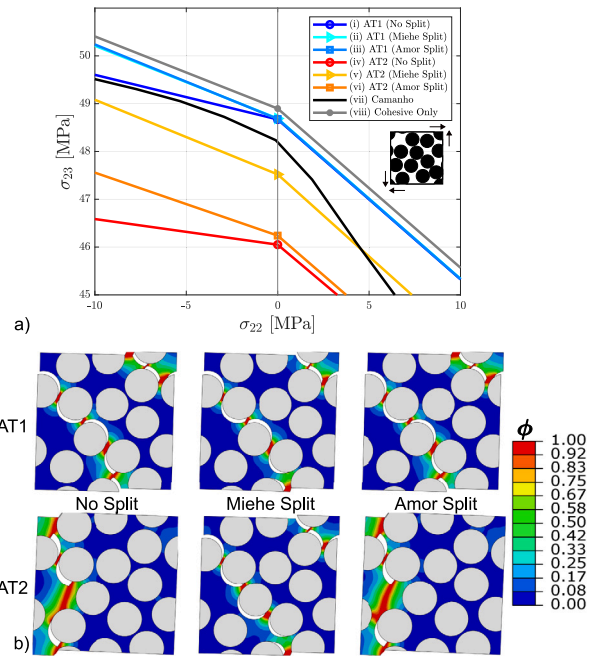

Fig. 12. (a) Failure envelopes and (b) crack patterns for pure compressive load of: (i) linear-elastic AT1 formulation without energy split, (ii) linear-elastic AT1 formulation with Miehe's energy split, (iii) linear-elastic AT1 formulation with Amor's energy split, (iv) linear-elastic AT2 formulation without energy split, (v) linear-elastic AT2 formulation with Miehe's energy split, (vi) linear-elastic AT2 formulation with Amor's energy split, (vii) Camanho et al. (2015) and (viii) linear-elastic matrix and cohesive interface damage (Cohesive Only). (For interpretation of the references to color in this figure legend, the reader is referred to the web version of this article.)

Fig. 13. (a) Failure envelopes and (b) crack patterns for pure transverse shear load of: (i) linear-elastic AT1 formulation without energy split, (ii) linear-elastic AT1 formulation with Miehe's energy split, (iii) linear-elastic AT1 formulation with Amor's energy split, (iv) linear-elastic AT2 formulation without energy split, (v) linear-elastic AT2 formulation with Miehe's energy split, (vi) linear-elastic AT2 formulation with Amor's energy split, (vii) Camanho et al. (2015) and (viii) linear-elastic matrix and cohesive interface damage (Cohesive Only). (For interpretation of the references to color in this figure legend, the reader is referred to the web version of this article.)

by decohesion or matrix damage. If the curves computed using a PF formulation are very close to the case *"Cohesive Only"*, then PF damage does not significantly affect the behavior of the RVE. As the length scale is further reduced, the curves approximate the *"Cohesive Only"* solution, showing that when the matrix strength is much higher than the interface strength, the maximum meso-scale stress is conditioned by the instability created by decohesion. The matrix fracture strength dictated by the length scale parameter and fracture toughness becomes relevant mainly for the post-peak behavior and is highly dependent on the loading scenario. Increasing the length scale brings the curves closer to the solution of Camanho et al. (2015) but the fracture-like pattern that represents a brittle fracture is gradually lost and replaced by a diffuse damage area whose physical interpretation can become ambiguous.

In the case of tensile loading, representative stress–strain curves for different lengths scales are shown in Fig. 15, and the crack patterns in Fig. 16. Maximum stress under this type of loading is fully dominated by the interface properties, as the peak is the same for all values of length scale and coincides with the peak stress of the *"Cohesive Only"* curve. The length scale mainly affects the post-peak behavior. In this case, a lower value of l_0 implies a higher strength, thus a material that fails gradually, while increasing l_0 promotes a brittle-like curve, similarly to increasing the size of a periodic RVE, proving that the study of material parameters can be highly dependent on the RVE size and BCs. In addition, increasing the length scale can change the damage pattern and prevent damage localization in an RVE micro-structure, thus, the damage pattern created by the PF variable does not resemble a crack like-pattern when the length scale is larger than 1 µm. This is observed even in the case of tensile loading, which is more prone to crack localization.

For transverse shear loading, representative stress–strain curves for different length scales are shown in Fig. 17, and the crack patterns in Fig. 18. The maximum stress under this type of loading is also
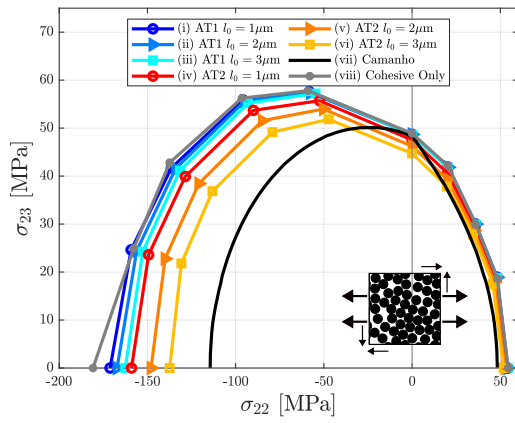
Fig. 14. Failure envelopes computed using: AT1 formulation with length scale (l_0) equal to (i) 1 μm, (ii) 2 μm, (iii) 3 μm, AT2 formulation with length scale equal to (iv) 1 μm, (v) 2 μm, (vi) 3 μm, (vii) Camanho et al. (2015) and (viii) linear-elastic matrix and cohesive interface damage (Cohesive Only) (for interpretation of the references to color in this figure legend, the reader is referred to the web version of this article).
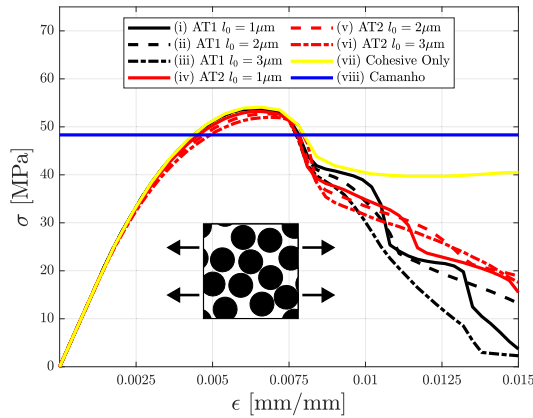

Fig. 17. Stress–strain curves for transverse shear loading using AT1 and AT2 formulations with length scale (l_0) equal to: (i) 1 μm, (ii) 2 μm and (iii) 3 μm and AT1 formulation, (iv) 1 μm, (v) 2 μm and (vi) 3 μm and AT2 formulation, (vii) linear-elastic matrix and cohesive interface damage (Cohesive Only) and (viii) strength according to Camanho et al. (2015). (For interpretation of the references to color in this figure legend, the reader is referred to the web version of this article.)
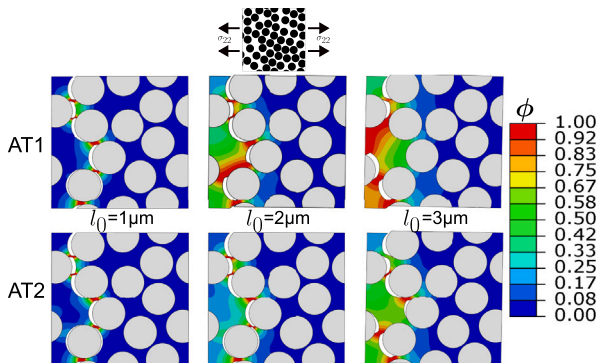

Fig. 15. Stress–strain curves for tensile loading using AT1 and AT2 formulations with length scale (l_0) equal to: (i) 1 μm, (ii) 2 μm and (iii) 3 μm and AT1 formulation, (iv) 1 μm, (v) 2 μm and (vi) 3 μm and AT2 formulation, (vii) linear-elastic matrix and cohesive interface damage (Cohesive Only) and (viii) strength according to Camanho et al. (2015). (For interpretation of the references to color in this figure legend, the reader is referred to the web version of this article.)

Fig. 18. Crack patterns for transverse shear loading using AT1 and AT2 formulations with length scale (l_0) equal to: (i) 1 μm, (ii) 2 μm and (iii) 3 μm. (For interpretation of the references to color in this figure legend, the reader is referred to the web version of this article.)

Fig. 16. Crack patterns for tensile loading using AT1 and AT2 formulations with length scale (l_0) equal to: (i) 1 μm, (ii) 2 μm and (iii) 3 μm. (For interpretation of the references to color in this figure legend, the reader is referred to the web version of this article.)

mainly dominated by fiber–matrix decohesion for the AT1 formulation, but matrix behavior is dominant in the AT2 formulation, because this formulation struggles to localize fracture under shear, as explained in Section 4.2. In this case, higher values of l_0 can modify the damage
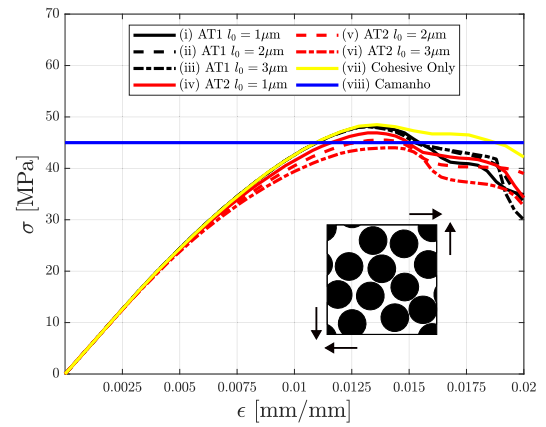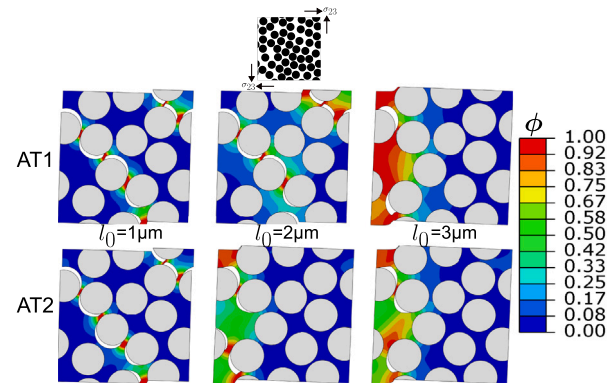
topology. For l_0 larger than 1 μm, the crack patterns coincident with the plane of maximum principal stresses can change to plastic-like damage patterns where damage follows the shear direction.

In the case of compressive loading, representative stress–strain curves for different lengths scales are shown in Fig. 19, and the crack patterns in Fig. 20. The maximum stress under this type of loading is dominated by the matrix behavior, but there is still matrix decohesion that can take place if the length scale is sufficiently small. The amount of decohesion decreases as the length scale increases, and the damage patterns for small values of l_0 go from crack-like patterns where decohesions are joined by small areas of matrix damage, to diagonal patches of matrix damage, with reduced damage at the interfaces for larger values of l_0.

4.4. Influence of the fiber–matrix interface on the failure envelope

The last verification involves removing the cohesive interface interaction and replacing it with a perfect bonding to study failure initiation triggered purely by PF damage. This is an assumption followed in previous micro-mechanical studies of composites using PF for pure transverse tension and pure transverse compression (Espadas-Escalante et al., 2019). In the case of tensile loading (Espadas-Escalante et al., 2019), it was found that the behavior was dominantly brittle even
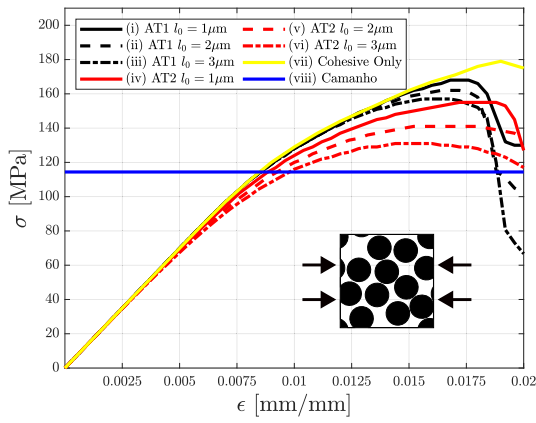
Fig. 19. Stress–strain curves for compressive loading using AT1 and AT2 formulations with length scale (l_0) equal to: (i) 1 µm, (ii) 2 µm and (iii) 3 µm and AT1 formulation, (iv) 1 µm, (v) 2 µm and (vi) 3 µm and AT2 formulation, (vii) linear-elastic matrix and cohesive interface damage (Cohesive Only) and (viii) strength according to Camanho et al. (2015). (For interpretation of the references to color in this figure legend, the reader is referred to the web version of this article.)

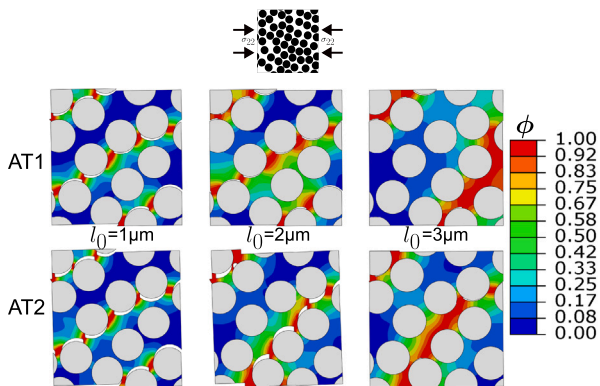**Fig. 20.** Crack patterns for compressive loading using AT1 and AT2 formulations with length scale (l_0) equal to: (i) 1 µm, (ii) 2 µm and (iii) 3 µm. (For interpretation of the references to color in this figure legend, the reader is referred to the web version of this article.)

for small RVEs, a behavior that can be attributed mainly to the very low matrix fracture toughness that was obtained from calibration in combination with the perfect interface bonding assumption. Fig. 8 compares the tensile stress–strain curves from RVEs with and without cohesive interface damage. All pairs of RVEs possess the same size and fiber distribution. It can be seen that, since cohesive damage is the first failure mechanism, removing the cohesive interaction implies a larger meso-scale strength. This trend can be perceived in transverse shear as well as compressive dominated loading, see Fig. 21. Failure envelopes computed using the matrix properties in Table 2 and ignoring interface damage lead to large overpredictions when compared with the failure criteria of Camanho et al. (2015), or the case of *"Cohesive Only"*.

5. Conclusions

The feasibility of the strength prediction of classical PF formulations and energy splits was assessed using RVE analyses for different fiber distributions, RVE sizes, loading conditions, PF parameters and interaction models. Using the PF method, reasonable predictions can be obtained but the accuracy is highly dependent on the energy split, PF formulation, length scale, and loading condition. Besides, the validity of the results can be limited by the difference between the length scale parameter and the geometric dimensions of the problem, especially if
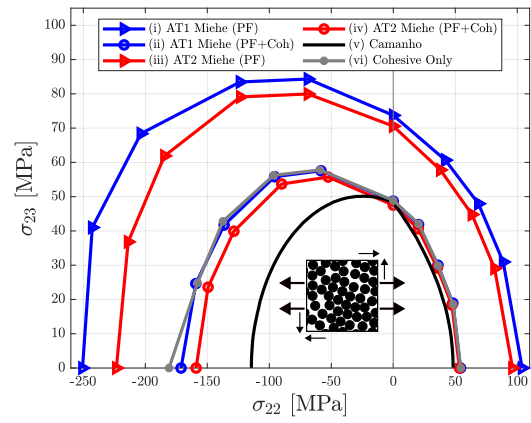

Fig. 21. Failure envelopes computed using: (i) AT1 formulation and Miehe's split accounting for perfect interface bonding, (ii) AT1 formulation and Miehe's split accounting for interface cohesive damage, (iii) AT2 formulation and Miehe's split accounting for perfect interface bonding, (iv) AT2 formulation and Miehe's split accounting for interface cohesive damage, (v) Camanho et al. (2015), and (vi) linear-elastic matrix and cohesive interface damage (Cohesive Only). (For interpretation of the references to color in this figure legend, the reader is referred to the web version of this article.)

the length scale is considered a strength-related property, which is the case of the formulations covered in this study.[3]

It was concluded that a square RVE of 0.08 mm side is necessary to obtain meaningful failure strain predictions, while accurate strength analyses can be performed with much smaller RVEs. It was also found that the AT2 formulation combined with Amor's energy split gives the closest prediction when compared to an analytical failure surface, while the AT1 formulation combined with Miehe's split yields the highest overprediction. Also, it is concluded that the accuracy of PF is highly affected by the loading scenario. The best fit was found for transverse shear-dominated loading, while larger differences were found for compressive loading, whose strength predictions are strongly affected by the PF formulations and energy splits. It was demonstrated that meso-scale strength is conditioned by interface properties since interface damage is the dominant failure initiation mechanism under tensile-dominated loading. In this case, matrix failure due to the PF formulation, length scale parameter and energy split are only relevant in terms of post-peak behavior (meso-scale toughness). On the other hand, PF parameters have a stronger influence on compressive-dominated loading. In this case, the AT2 formulation generally leads to failure envelopes closer to the analytical reference solutions. Moreover, accounting for fiber–matrix interface damage defines a threshold curve from which PF parameters stop exerting influence on meso-scale strength. Finally, it was shown that assuming a perfect fiber–matrix interface has a strong effect on the expected meso-scale strength, as failure is delayed but the apparent behavior becomes more brittle.

This work thus provides useful guidance to the selection of classical PF formulations and energy splits for computational micro-mechanical analyses for general stress states considering 2D plane strain assumptions and matrix linear-elastic behavior. Further analyses, using 3D models to assess the effects of crack tunneling, and a nonlinear, plastic matrix behavior, are required to complement these conclusions.

---

[3] The use of the PF-CZM formulation developed by Wu and Nguyen (2018) would allow reducing the length scale to micro-scale dimensions while defining an elastic threshold based on energy criteria instead of the length scale parameter, in other words, explicitly defining the strength independently of the length scale parameter. For this reason, the PF-CZM formulation is not assessed in this study, with the focus turned to the classical AT1 and AT2 formulations.

In addition, more detailed analyses, incl. larger RVEs, can be explored to obtain longer crack patterns and predict in more detail the fracture angles, in particular for comparison with other ply failure criteria (Puck and Schürmann, 2002). Finally, particularizing the phase-field formulation to specific failure surfaces, incl. pressure-dependent behavior (Azinpour et al., 2021; Navidtehrani et al., 2022), could result in interesting avenues to minimize or overcome the dependency of the solutions on the model parameters and loading condition.

CRediT authorship contribution statement

Juan Macías: Conceptualization, Methodology, Implementation, Analysis, Writing – original draft, Writing – review & editing. **Albertino Arteiro:** Conceptualization, Methodology, Analysis, Writing – review & editing. **Fermín Otero:** Conceptualization, Methodology, Analysis, Writing – review & editing. **Pedro P. Camanho:** Conceptualization, Methodology, Analysis, Writing – review & editing. **José Reinoso:** Conceptualization, Methodology, Analysis, Writing – review & editing.

Declaration of competing interest

The authors declare that they have no known competing financial interests or personal relationships that could have appeared to influence the work reported in this paper.

Data availability

No data was used for the research described in the article.

Acknowledgments

References

Amor, Hanen, Marigo, Jean-Jacques, Maurini, Corrado, 2009. Regularized formulation of the variational brittle fracture with unilateral contact: Numerical experiments. J. Mech. Phys. Solids 57 (8), 1209–1229.

Anon, 2022. Digimat - The Composite materials modeling Software.

Arteiro, A., Catalanotti, G., Melro, A.R., Linde, P., Camanho, P.P., 2014. Micromechanical analysis of the in situ effect in polymer composite laminates. Compos. Struct. 116, 827–840.

Azinpour, Erfan, de Sa, Jose Cesar, dos Santos, Abel Dias, 2021. Micromechanically-motivated phase field approach to ductile fracture. Int. J. Damage Mech. 30 (1), 46–76.

Bourdin, B., Francfort, G.A., Marigo, J.-J., 2000. Numerical experiments in revisited brittle fracture. J. Mech. Phys. Solids 48 (4), 797–826.

Camanho, P.P., Arteiro, A., Melro, A.R., Catalanotti, G., Vogler, M., 2015. Three-dimensional invariant-based failure criteria for fibre-reinforced composites. Int. J. Solids Struct. 55, 92–107.

Canal, Luis Pablo, González, Carlos, Segurado, Javier, Llorca, Javier, 2012. Intraply fracture of fiber-reinforced composites: Microscopic mechanisms and modeling. Compos. Sci. Technol. 72 (11), 1223–1232.

Coenen, E.W.C., Kouznetsova, V.G., Bosco, E., Geers, M.G.D., 2012a. A multi-scale approach to bridge microscale damage and macroscale failure: a nested computational homogenization-localization framework. Int. J. Fract. 178 (1), 157–178.

Coenen, E.W.C., Kouznetsova, V.G., Geers, M.G.D., 2012b. Novel boundary conditions for strain localization analyses in microstructural volume elements. Internat. J. Numer. Methods Engrg. 90, 1–21.

Danzi, F., Fanteria, D., Panettieri, E., Palermo, M., 2017. A numerical micro-mechanical study of the influence of fiber–matrix interphase failure on carbon/epoxy material properties. Compos. Struct. 159, 625–635.

Espadas-Escalante, J.J., van Dijk, N.P., Isaksson, P., 2019. A phase-field model for strength and fracture analyses of fiber-reinforced composites. Compos. Sci. Technol. 174, 58–67.

Francfort, Gilles A., Bourdin, Blaise, Marigo, Jean Jacques, 2008. The variational approach to fracture. J. Elasticity 91 (1), 5–148.

Francfort, G.A., Marigo, J.-J., 1998. Revisiting brittle fracture as an energy minimization problem. J. Mech. Phys. Solids 46 (8), 1319–1342.

Griffith, A.A., 1921. The phenomena of rupture and flow in solids. Philos. Trans. R. Soc. Lond. Ser. A Contain. Pap. Math. Phys. Charact. 221, 163–198.

Guillén-Hernández, T., García, I.G., Reinoso, J., Paggi, M., 2019. A micromechanical analysis of inter-fiber failure in long reinforced composites based on the phase field approach of fracture combined with the cohesive zone model. Int. J. Fract. 220 (2), 181–203.

Guillén-Hernández, T., Quintana-Corominas, A., García, I.G., Reinoso, J., Paggi, M., Turón, A., 2020. In-situ strength effects in long fibre reinforced composites: A micro-mechanical analysis using the phase field approach of fracture. Theor. Appl. Fract. Mech. 108, 102621.

Hinton, MJ.K.A., Soden, P.D., Kaddour, Abdul-Salam, 2004. Failure Criteria in Fibre Reinforced Polymer Composites: The World-Wide Failure Exercise. Elsevier.

Kristensen, Philip K., Martínez-Pañeda, Emilio, 2020. Phase field fracture modelling using quasi-Newton methods and a new adaptive step scheme. Theor. Appl. Fract. Mech. 107, 102446.

Kristensen, Philip K., Niordson, Christian F., Martínez-Pañeda, Emilio, 2021. An assessment of phase field fracture: crack initiation and growth. Phil. Trans. R. Soc. A 379.

Li, Pengfei, Yvonnet, Julien, Combescure, Christelle, 2020. An extension of the phase field method to model interactions between interfacial damage and brittle fracture in elastoplastic composites. Int. J. Mech. Sci. 179, 105633.

Marigo, J.-J., Maurini, C., Pham, K., 2016. An overview of the modelling of fracture by gradient damage models. Meccanica 51 (12), 3107–3128.

Martínez-Pañeda, Emilio, Golahmar, Alireza, Niordson, Christian F., 2018. A phase field formulation for hydrogen assisted cracking. Comput. Methods Appl. Mech. Engrg. 342, 742–761.

Melro, A.R., Camanho, P.P., Andrade Pires, F.M., Pinho, S.T., 2013. Micromechanical analysis of polymer composites reinforced by unidirectional fibres: Part II – micromechanical analyses. Int. J. Solids Struct. 50 (11), 1906–1915.

Miehe, C., Welschinger, F., Hofacker, M., 2010. Thermodynamically consistent phase-field models of fracture: Variational principles and multi-field FE implementations. Internat. J. Numer. Methods Engrg. 83, 1273–1311.

Navidtehrani, Yousef, Betegón, Covadonga, Martínez-Pañeda, Emilio, 2021a. A simple and robust abaqus implementation of the phase field fracture method. Appl. Eng. Sci. 6, 100050.

Navidtehrani, Yousef, Betegón, Covadonga, Martínez-Pañeda, Emilio, 2021b. A unified Abaqus implementation of the phase field fracture method using only a user material subroutine. Materials 14 (8).

Navidtehrani, Yousef, Betegón, Covadonga, Martínez-Pañeda, Emilio, 2022. A general framework for decomposing the phase field fracture driving force, particularised to a Drucker–Prager failure surface. Theor. Appl. Fract. Mech. 121, 103555.

Pineda, Evan J., Bednarcyk, Brett A., Waas, Anthony M., Arnold, Steven M., 2013. Progressive failure of a unidirectional fiber-reinforced composite using the method of cells: Discretization objective computational results. Int. J. Solids Struct. 50 (9), 1203–1216.

Puck, A., Schürmann, H., 2002. Failure analysis of FRP laminates by means of physically based phenomenological models. Compos. Sci. Technol. 62 (12), 1633–1662.

Quintanas-Corominas, A., Reinoso, J., Casoni, E., Turon, A., Mayugo, J.A., 2019. A phase field approach to simulate intralaminar and translaminar fracture in long fiber composite materials. Compos. Struct. 220, 899–911.

Saito, Hiroshi, Takeuchi, Hiroki, Kimpara, Isao, 2012. Experimental evaluation of the damage growth restraining in 90° layer of thin-ply CFRP cross-ply laminates. Adv. Compos. Mater. 21 (1), 57–66.

Song, Leying, Meng, Songhe, Xu, Chenghai, Fang, Guodong, Yang, Qiang, Xie, Weihua, 2020. Crack kinking and tunneling simulation for the single-fiber composite under transverse tension based on phase-field method. J. Strain Anal. Eng. Des. 55 (5–6), 145–158.

Sun, Qingping, Meng, Zhaoxu, Zhou, Guowei, Lin, Shih-Po, Kang, Hongtae, Keten, Sinan, Guo, Haiding, Su, Xuming, 2018. Multi-scale computational analysis of unidirectional carbon fiber reinforced polymer composites under various loading conditions. Compos. Struct. 196, 30–43.

Svenning, Erik, Fagerström, Martin, Larsson, Fredrik, 2017. Localization aligned weakly periodic boundary conditions. Internat. J. Numer. Methods Engrg. 111 (5), 493–500.

Tan, Wei, Martínez-Pañeda, Emilio, 2021. Phase field predictions of microscopic fracture and R-curve behaviour of fibre-reinforced composites. Compos. Sci. Technol. 202, 108539.

Tan, Wei, Martínez-Pañeda, Emilio, 2022. Phase field fracture predictions of microscopic bridging behaviour of composite materials. Compos. Struct. 286, 115242.

Tan, W., Naya, F., Yang, L., Chang, T., Falzon, B.G., Zhan, L., Molina-Aldareguía, J.M., González, C., Llorca, J., 2018. The role of interfacial properties on the intralaminar and interlaminar damage behaviour of unidirectional composite laminates: Experimental characterization and multiscale modelling. Composites B 138, 206–221.

Totry, Essam, González, Carlos, Llorca, Javier, 2008a. Failure locus of fiber-reinforced composites under transverse compression and out-of-plane shear. Compos. Sci. Technol. 68 (3), 829–839.

Totry, Essam, González, Carlos, Llorca, Javier, 2008b. Prediction of the failure locus of c/PEEK composites under transverse compression and longitudinal shear through computational micromechanics. Compos. Sci. Technol. 68 (15), 3128–3136.

Trias, D., Costa, J., Turon, A., Hurtado, J.E., 2006. Determination of the critical size of a statistical representative volume element (SRVE) for carbon reinforced polymers. Acta Mater. 54 (13), 3471–3484.

van der Meer, Frans P., 2016. Micromechanical validation of a mesomodel for plasticity in composites. Eur. J. Mech. A Solids 60, 58–69.

Vaughan, T.J., McCarthy, C.T., 2011. Micromechanical modelling of the transverse damage behaviour in fibre reinforced composites. Compos. Sci. Technol. 71 (3), 388–396.

Wu, Jian-Ying, Huang, Yuli, 2020. Comprehensive implementations of phase-field damage models in Abaqus. Theor. Appl. Fract. Mech. 106, 102440.

Wu, Jian-Ying, Nguyen, Vinh Phu, 2018. A length scale insensitive phase-field damage model for brittle fracture. J. Mech. Phys. Solids 119, 20–42.

Wu, Jian-Ying, Nguyen, Vinh Phu, Thanh Nguyen, Chi, Sutula, Danas, Bordas, Stéphane, Sinaie, Sina, 2019. Phase field modelling of fracture. Adv. Appl. Mech. 53, 1–183.

Yin, B.B., Zhang, L.W., 2019. Phase field method for simulating the brittle fracture of fiber reinforced composites. Eng. Fract. Mech. 211, 321–340.

Zhang, Peng, Hu, Xiaofei, Bui, Tinh Quoc, Yao, Weian, 2019. Phase field modeling of fracture in fiber reinforced composite laminate. Int. J. Mech. Sci. 161–162, 105008.

Zhang, Peng, Yao, Weian, Hu, Xiaofei, Bui, Tinh Quoc, 2020. 3D micromechanical progressive failure simulation for fiber-reinforced composites. Compos. Struct. 249, 112534.